Computer Modeling in Engineering & Sciences

Tech Science Press

https://doi.org/10.32604/cmes.2026.084886

ARTICLE

Numerical Study of the Vaporization and Combustion of Single *p*-Xylene Droplets in Hot Air

Sachin Tom and Eva Gutheil*

Interdisciplinary Center for Scientific Computing, Heidelberg University, Heidelberg, Germany

*Corresponding Author: Eva Gutheil. Email: gutheil@iwr.uni-heidelberg.de

Received: 30 April 2026; Accepted: 05 June 2026; Published: 27 July 2026

ABSTRACT: A single droplet heating, vaporization, and detailed combustion model is developed for pure *p*-xylene (*p*-C_8H_{10}) in hot air. *p*-C_8H_{10} is a combustible solvent in precursor solutions, for instance, with titanium tetraisopropoxide (TTIP) for the production of TiO_2 nanoparticles. In the present one-dimensional mathematical model, a spherically symmetric *p*-xylene droplet in hot air is considered, resolving both the droplet (liquid phase) and the ambience (gas phase). The calculation of the vaporization rate includes the Stefan velocity at the droplet surface. In the gas phase, a detailed chemical reaction scheme is used. Elementary reactions are combined with complex reactions that account for the thermal decomposition of the *p*-xylene. The reaction mechanism comprises 93 chemical reactions among 25 species. Variable thermo-physical properties are used for both the gas and the liquid phase. A parameter study is conducted by varying the hot ambient gas temperature and the initial droplet size. In a hot ambience, initial expansion of the *p*-xylene droplet occurs due to droplet heating. After initial heating and vaporization, autoignition and combustion in the gas phase take place. In contrast to similar studies of single droplet combustion in the literature, the present simulations are not only carried to the end of the droplet lifetimes but continued until the gas flame extinguishes due to lack of combustible fuel. The vaporization rate constant, the autoignition, and the flame standoff distance are analyzed.

KEYWORDS: Single droplet vaporization; *p*-xylene droplet; autoignition; combustion; detailed chemical reactions

1 Introduction

Nanoparticle synthesis through combustion processes [1] has achieved growing attention based on its industrial applications, for instance, in agriculture, healthcare, pharmaceuticals, electronics, and cosmetics. *p*-Xylene (*p*-C_8H_{10}) is commonly used as a combustible solvent in precursor solutions in these processes, for instance, with titanium tetraisopropoxide (TTIP) because they do not chemically react in the liquid phase. Flame Spray Pyrolysis (FSP) involving the TTIP/*p*-xylene precursor solution results in the formation of TiO_2 nanoparticles with a wide industrial use. The TTIP/*p*-xylene droplet undergoes vaporization, autoignition, and combustion, and puffing and micro-explosions may occur before the formation of the TiO_2 nanoparticles [2–4]. Thus, the understanding of single-component pure *p*-xylene droplet combustion is interesting before the study of bi-component TTIP/*p*-xylene precursor solution droplets.

There is a vast amount of literature for single-droplet vaporization and combustion, ranging from very simple models such as the d^2-law [5] to more advanced models considering droplet heating and expansion and variable liquid properties using zero-dimensional, one-, two-, and three-dimensional models with different degrees of complexity [6]. In early studies, the gas phase model is not resolved, and mainly,

Copyright © 2026 The Authors. Published by Tech Science Press. This work is licensed under a Creative Commons Attribution 4.0 International License, which permits unrestricted use, distribution, and reproduction in any medium, provided the original work is properly cited.

the droplet vaporization is considered. The combustion process may be simplified by using infinitely fast chemistry [7] or one-step reactions [8]. The consideration of autoignition or spark ignition in the gas phase is considered using different complexities of chemical reaction schemes [9].

Both experimental and computational studies of single-component droplet combustion under microgravity conditions in a quiescent ambience exist. In the numerical studies, most often spherically symmetric droplets are assumed. Both the droplet interior and exterior regions may be resolved. Cho et al. [10] developed a mathematical model for a single droplet vaporization and combustion. The mass, species, and energy transport equations are solved with both detailed transport properties and detailed chemical kinetics. The model is used to investigate the oxidation of carbon particles, combustion of methanol droplets, and the chemically facilitated vaporization of liquid boron oxide droplets. Marchese and Dryer [11] employed a one-dimensional mathematical model for the combustion and extinction of single methanol and bi-component methanol/water droplets in ambient air with detailed chemical reactions. The numerical results are compared with those of the experiments, where a free-falling single droplet was analyzed in a microgravity drop tower. Major combustion and ignition characteristics, as well as the flame standoff distance computed from the numerical simulations, are compared with the experimental results.

A one-dimensional mathematical model for the unsteady vaporization, ignition, and combustion of a fuel droplet with detailed chemical kinetics is developed by Cuoci et al. [12]. They predicted the autoignition and vaporization rates of a single isolated *n*-decane droplet at hot ambient conditions but neglected a soot model, which might be relevant in aromatic droplet burning. Their simple radiation model showed some effect on the temperature profiles for large droplet burning. Later work addressing aromatic droplet burning [13] included both soot formation and radiation, which showed a retardation of the combustion since both reduce the flame temperature.

Giusti et al. [14] analyzed the autoignition behavior of kerosene droplets under gas turbine conditions and predicted the flame structures for a wide range of dilution levels of ambient air with hot combustion products and at different initial droplet diameters. Zhang et al. [15] performed one-dimensional numerical simulations for the autoignition of *n*-heptane droplets in microgravity conditions. They investigated the fundamental mechanisms for the presence of four boundaries on the temperature-pressure (T-P) diagram for ambient temperature from 600 to 1000 K and ambient pressures from 1 to 20 bar. Their HILL (Hot Ignition Lower Limit) is relevant in the present study.

Chen et al. [16] performed a combined experimental and theoretical study for a variety of alkanes and alcohols of low and high-boiling hydrocarbons under gravity. They corrected the d^2 law to a d^n law and found that the exponent n varies from 2.53 to 2.69 for these fuels. This non-square power law is found to be a consequence of simultaneous momentum, heat, and mass transfer resulting from buoyant convection by the blazing flame around the droplet.

A theoretical study of pure *m*-xylene single droplet combustion under spark ignition conditions with single step global reaction has been carried out by Ren et al. [17]. A simplified model assuming the Burke-Schumann limit for the combustion is considered here with the assumption of unity gas-phase Lewis numbers. Kunstmann et al. [4] studied superheating in evaporating droplets for spray flame synthesis. They have developed a droplet vaporization model for pure *p*-xylene, but the combustion process is not modeled in their work.

Among the experimental works for single droplet combustion, Rosebrock et al. [18] investigated the combustion characteristics of isolated precursor/solvent droplets. The droplet is injected into the coflowing oxygen, and after the spark ignition by the electrodes, the combustion is monitored with a high-speed camera. The pure *p*-xylene solvent droplet combustion behavior is studied. They also discuss the high

sooting tendency of *p*-xylene. Li et al. [2] used high-end optical techniques such as interferometric particle imaging and standard rainbow refractometry to analyze the single droplet combustion. A pure *p*-xylene droplet combustion experiment was performed, and the isolated burning droplet images were captured at different time instants. They also found soot formation surrounding the burning droplet and identified the droplet lifetime. Shang et al. [19] performed single droplet combustion experiments of *n*-hexadecane droplets using the two optical techniques of natural flame luminosity imaging and diffused back-illumination extinction imaging (DBIEI). Both premixed and non-premixed combustion periods were identified, and the results demonstrated that the DBIEI technique is capable of quantitatively measuring the instantaneous soot formation during droplet combustion.

Thus, there is a lack of a model that describes the entire process of droplet heating, vaporization, autoignition, and combustion with detailed chemical kinetics in hot ambient air, all the way until the chemical reactions break down.

In the present study, single *p*-xylene droplet heating, vaporization, and combustion are considered in a hot quiescent ambient air environment. The autoignition and combustion are modeled using a detailed chemical reaction scheme with some complex reactions. The numerical simulations are carried beyond the droplet lifetime until the chemical reactions break down due to a lack of combustible fuel vapor. Thus, the scope of the study is an improved understanding of the autoignition and combustion characteristics of these droplets.

2 Mathematical Model

The mathematical model describes the combustion of an isolated fuel droplet in a hot quiescent gas environment. The following assumptions are taken into account:

- spherically symmetric droplets and absence of natural and forced convection effects
- constant ambient pressure
- absence of liquid-phase reactions
- thermodynamic equilibrium at the liquid-gas interface
- no thermal radiation
- negligible Soret and Dufour effects
- low Mach number.

With these assumptions, the system can be formulated in spherical one-dimensional time-dependent equations. The governing equations and the boundary and initial conditions are provided in the next subsections.

2.1 Liquid-Phase Equations

With the definition of the mass vaporization rate $\dot{m}$

$$\dot{m} = -\frac{dm}{dt} = -\frac{d}{dt}\left(\frac{4}{3}\pi r_s^3 \rho_l\right), \tag{1}$$

where m and t denote the droplet mass and the time, respectively, the index 's' shows conditions at the droplet surface, r_s is the actual droplet radius, and the subscript 'l' denotes liquid properties. ρ_l is the liquid density, the mass vaporization rate of the droplet is given as [12]

$$\dot{m} = \rho\left(u - \frac{dr_s}{dt}\right)4\pi r_s^2. \tag{2}$$

In the above equation, ρ is the gas density, and u denotes the gas velocity.

Droplet heating is described considering the heat conduction inside the droplet as

$$\frac{\partial}{\partial t}\left(\rho_{\mathrm{l}} c_{\mathrm{pl}} T_{\mathrm{l}}\right) = \frac{1}{r^2}\frac{\partial}{\partial r}\left(r^2 \lambda_{\mathrm{l}} \frac{\partial T_{\mathrm{l}}}{\partial r}\right), \tag{3}$$

where c_{pl} is the specific heat capacity of the liquid at constant pressure, T_{l} is the liquid temperature, and r denotes the radial direction. The liquid thermal conductivity is λ_{l}.

2.2 Gas-Phase Equations

Under the present conditions, the momentum equation is trivially fulfilled [6] and the continuity equation includes the Stefan velocity u. The continuity equation is given by

$$\frac{\partial \rho}{\partial t} + \frac{1}{r^2}\frac{\partial}{\partial r}\left(r^2 \rho u\right) = 0, \tag{4}$$

where ρ is gas density and r is radial direction.

The energy equation is written as

$$\frac{\partial}{\partial t}\left(\rho c_{\mathrm{p}} T\right) = -\frac{1}{r^2}\frac{\partial}{\partial r}\left(r^2 \rho u c_{\mathrm{p}} T\right) + \frac{1}{r^2}\frac{\partial}{\partial r}\left(r^2 \lambda \frac{\partial T}{\partial r}\right) + \rho \frac{\partial T}{\partial r}\left(\sum_{k=1}^{N} c_{\mathrm{p,k}} D_k \frac{\partial Y_k}{\partial r}\right) - \sum_{k=1}^{N} M_k \dot{\omega}_k h_k, \tag{5}$$

where D_k is the diffusion coefficient of species k into the gas mixture, $c_{\mathrm{p},k}$ is the specific heat capacity at constant pressure of species k, and h_k and M_k are the specific enthalpy and the molecular mass of species k, respectively. The chemical reaction rate of species k is denoted by $\dot{\omega}_k$, $k = 1, \ldots, N$ for the N species.

The conservation of species mass fractions Y_k, $k = 1, \ldots, N$ is given by

$$\frac{\partial}{\partial t}\left(\rho Y_k\right) = -\frac{1}{r^2}\frac{\partial}{\partial r}\left(r^2 \rho u Y_k\right) + \frac{1}{r^2}\frac{\partial}{\partial r}\left(r^2 \rho D_k \frac{\partial Y_k}{\partial r}\right) + M_k \dot{\omega}_k. \tag{6}$$

The chemical reaction scheme derived by Nanjaiah et al. [20] with 25 chemical species and 93 chemical reactions is used, containing both detailed and complex reactions; the mechanism was reduced from the detailed chemical reaction mechanism of Ranzi et al. [21]. Soot formation is not included in that chemical reaction scheme. However, soot precursors are considered, which will allow for future predictions of soot formation. Moreover, radiation is not considered since it is found to have a major influence only for large droplet burning [12].

The present droplet vaporization model was validated in the previous studies of Narasu et al. [22] who studied *p*-xylene vaporization in an infinite ambience of air. The mass evaporation model of Cuoci et al. [12] is used for the resolution of the ambience of the droplet, and it was validated for the autoignition of *n*-heptane droplets in air. The chemical reaction scheme derived by Nanjaiah et al. [20] has been successfully used for the simulation of the combustion of *p*-xylene sprays in the counterflow configuration [23].

All liquid- and gas-phase properties are variable, and they are evaluated following earlier work [22,24]. The boundary conditions are as follows.

2.3 Boundary and Initial Conditions

The system has three different boundaries, one is at the droplet interior at $r = 0$, another one at the droplet surface, $r = r_{\mathrm{s}}$, and in the 'infinite' ambience of the gas phase, $r = \infty$.

2.3.1 At the Droplet Center $(r = 0)$

The boundary condition for the liquid temperature at the droplet center is

$$\left.\frac{\partial T_{\mathrm{l}}(r,t)}{\partial r}\right|_{r=0} = 0, \tag{7}$$

and the initial condition at $t = 0$ is

$$\left.T_{\mathrm{l}}(r,t)\right|_{t=0} = T_{\mathrm{l},0}. \tag{8}$$

The initial temperature $T_{\mathrm{l},0}$ equals 300 K.

2.3.2 At the Droplet Surface $(r = r_s)$

The vaporization velocity at the droplet surface [25] is

$$\left.u\right|_{r=r_{\mathrm{s}}} = \frac{D_{\mathrm{F,s}}\left.\frac{\partial Y_{\mathrm{F}}}{\partial r}\right|_{r=r_{\mathrm{s}}}}{Y_{\mathrm{F,s}} - 1}, \tag{9}$$

where the index 'F' denotes properties of the fuel vapor.

The gas and liquid temperatures are equal at the droplet surface

$$\left.T\right|_{r=r_s} = \left.T_{\mathrm{l}}\right|_{r=r_s}. \tag{10}$$

The energy balance at the droplet surface can be written as [26]

$$\left.\frac{\partial(\lambda T)}{\partial r}\right|_{r=r_{\mathrm{s}}} = \left.\frac{\partial(\lambda_{\mathrm{l}} T_{\mathrm{l}})}{\partial r}\right|_{r=r_{\mathrm{s}}} + \dot{m} L_{\mathrm{v}}(T_{\mathrm{s}}), \tag{11}$$

where $L_{\mathrm{v}}(T_{\mathrm{s}})$ is the temperature-dependent latent heat of vaporization.

The mole fraction of the fuel vapor at the droplet surface is

$$X_{\mathrm{F,s}} = \frac{p_{\mathrm{v}}}{p_{\infty}}, \tag{12}$$

where the vapor pressure at the droplet surface, p_{v}, is determined from the Antoine equation

$$\log_{10} p_{\mathrm{v}} = A - \frac{B}{C + T_{\mathrm{s}}}. \tag{13}$$

The values A, B and C are provided by Keller et al. [24]. In Eq. (12), p_{∞} denotes the ambient pressure, which is atmospheric in the present study.

2.3.3 In the Far Field $(r = r_{\infty})$

The boundary conditions are

$$\left.\frac{\partial T}{\partial r}\right|_{r=r_{\infty}} = 0; \quad \left.\frac{\partial u}{\partial r}\right|_{r=r_{\infty}} = 0; \quad \left.\frac{\partial Y_k}{\partial r}\right|_{r=r_{\infty}} = 0,\ k = 1, \ldots, N. \tag{14}$$

The initial conditions in the far field are

$$\left.T(r,t)\right|_{t=0} = T_{\infty};\ \left.u(r,t)\right|_{t=0} = 0.0;\ \left.Y_{\mathrm{N_2}}(r,t)\right|_{t=0} = 0.767;\ \left.Y_{\mathrm{O_2}}(r,t)\right|_{t=0} = 0.233, \tag{15}$$

i.e., the droplets are in an ambience of air. The values of T_∞ and $r_{s,0}$ are varied and will be provided in the results section.

The liquid and gas phase equations are strongly coupled and require numerical solution.

2.4 Numerical Solution Procedure

The liquid and the gas phase equations are solved simultaneously. An in-house computer code in the programming language *C* has been developed for the single droplet combustion simulations. The numerical scheme is an extension of earlier work [22] where the gas phase was not resolved.

Explicit time marching is adopted, and central differencing is used to discretize the governing equations for the liquid and the gas phases. The numerical time step size for the liquid and gas phases is 10^{-10} s to fulfill the Courant criterion. The explicit time marching scheme requires such small time steps but it captures the highly transient ignition and flame dynamics and resolves the small time-scales during the ignition.

The droplet vaporization is assumed to be completed when the relative droplet radius $r_s/r_{s,0}$ has reached a value of 10^{-3}, which refers to 10^{-9} of the initial droplet mass. The simulations are continued in the gas phase until the flame extinguishes to predict the droplet burnout stage.

The spatial grid inside the droplet consists of 10 uniform grid points for the droplet interior, where simulations with 20 grid points showed no significant difference compared to the 10 grid points used in the present study [22]. The computational domain of the gas phase is taken approximately 100 times the initial droplet radius, $r_{s,0}$ [14]. The numerical grid consists of about $M = 250$ grid nodes. Different non-uniform meshes with increasing grid spacing from the droplet surface following $\Delta r_{i+1} = (1+\epsilon)\Delta r_i$, $i = 1\ldots, K$ are investigated to ensure grid independence. The grid size r_g of the gas phase normalized by the initial droplet size $r_{s,0}$ yields

$$\frac{r_g}{r_{s,0}} = \Delta r_1 \frac{(1+\epsilon)^{M-1} - 1}{\epsilon}. \tag{16}$$

The parameter ϵ is varied between 0.020 and 0.025 and the initial grid cell Δr_1 between 0.3 and 0.75 µm. It is found that the values $\epsilon = 0.025$ and $\Delta r_1 = 0.5$ µm are appropriate for an initial droplet radius of 100 µm and an ambient gas temperature, T_∞ of 1500 K, cf. Table 1, as shown in Figs. 1 and 2.

Table 1: Conditions for the study of grid independence, cf. Eq. (16).

Case	ϵ	Δr_1 [µm]	M	$r_g/r_{s,0}$	τ_{ig} [ms]	τ_{ig}/d_0^2 [µs/µm^2]	τ_d [ms]	τ_d/d_0^2 [µs/µm^2]	τ_t [ms]	τ_t/d_0^2 [µs/µm^2]
1	0.020	0.50	300	93	3.00	0.075	25.90	0.65	45.30	1.13
2	0.020	0.75	300	140	3.10	0.077	25.90	0.65	46.10	1.15
3	0.025	0.50	250	93	3.00	0.075	25.90	0.65	45.10	1.12
4	0.025	0.30	275	104	3.00	0.075	25.90	0.65	43.30	1.08

Table 1 shows the ignition time τ_{ig}, the droplet lifetime τ_d, and the total process time τ_t in dimensional units and divided by the square of the initial droplet diameter d_0^2. From Figs. 1 and 2, which show the profiles of the gas temperature at different times for the four cases, it can be seen that case 3 seems to be the best choice for the parameters shown in Table 1.

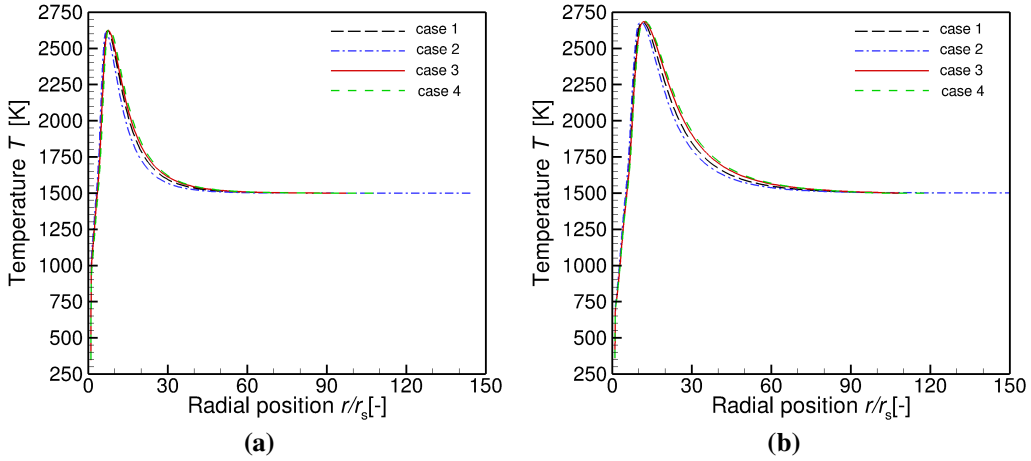

Figure 1: Spatial variation of gas temperature at (**a**) t/d_0^2 = 0.125 µs/µm^2 and (**b**) t/d_0^2 = 0.25 µs/µm^2.

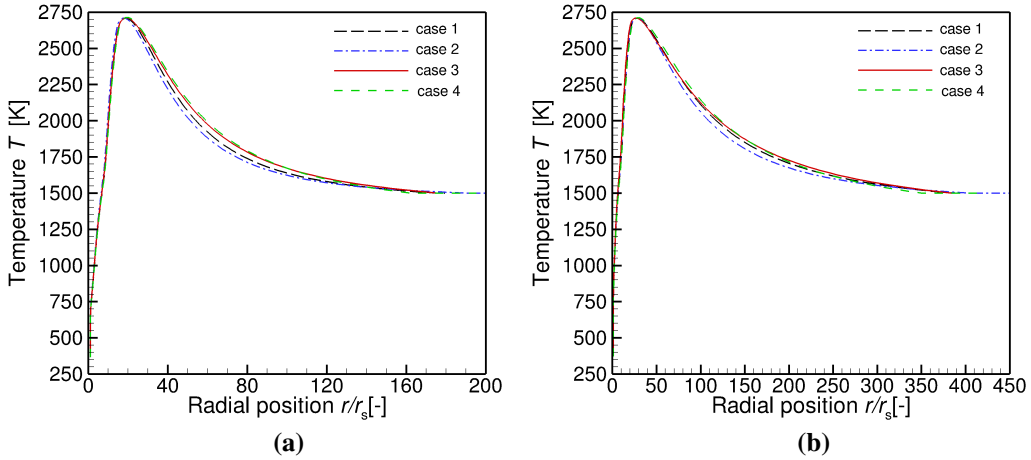

Figure 2: Spatial variation of gas temperature at (**a**) t/d_0^2 = 0.5 µs/µm^2 and (**b**) t/d_0^2 = 0.625 µs/µm^2.

For smaller initial droplet sizes studied in the remainder of the paper, the value of Δr_1 is reduced accordingly and that of ϵ is reduced to achieve a computational domain of about 100 $r_{s,0}$ while the other parameters are fixed.

3 Results and Discussion

A parameter study of single *p*-xylene droplets in hot air is performed, where droplet heating, vaporization, ignition, and combustion, including the burnout stage of the droplet, are considered. The pressure in all simulations is atmospheric, and the initial droplet temperature is fixed at $T_{l,0}$ = 300 K. The hot ambient temperature is varied from T_∞ = 1500 to 1400 K and to 1300 K, cf. Eq. (15), and the initial droplet radius is doubled from $r_{s,0}$ = 43 to 86 µm; these values are taken from the experiment of Li et al. [2]. Table 2 shows the different conditions studied in the present paper. Moreover, the ignition time τ and the droplet lifetime τ_d are shown. Many studies display the droplet characteristics in terms of τ_d/d_0^2, which is also listed in the Table 2. Moreover, τ_t is the total process time, i.e., it includes the droplet burnout stage.

Table 2: Initial ambient gas temperature T_∞ and droplet radius $r_{s,0}$ as well as ignition time τ_{ig}, droplet lifetime τ_d, and total process time τ_t for the conditions under investigation.

Case	T_∞ [K]	$r_{s,0}$ [µm]	τ_{ig} [ms]	τ_{ig}/d_0^2 [µs/µm^2]	τ_d [ms]	τ_d/d_0^2 [µs/µm^2]	τ_t [ms]	τ_t/d_0^2 [µs/µm^2]
A	1500	43	0.70	0.10	5.10	0.69	12.80	1.73
B	1400	43	0.95	0.13	5.52	0.74	13.50	1.82
C	1300	43	1.50	0.20	5.85	0.79	14.60	1.97
D	1500	86	2.10	0.07	19.75	0.66	38.40	1.30

There is no experimental data for direct comparison with the present numerical simulations. The single-droplet experiment of Li et al. [2] was performed in an ambience of 100% oxygen, whereas the present simulations use air. The droplet vaporization model, however, was verified in earlier studies [3,22], and the chemical reaction scheme for *p*-xylene in air was also successfully used in spray flame simulations in the counterflow configuration [23]. Exploratory simulations show reasonable agreement with the experimental data for a non-reacting ambience, see also the discussion below.

In the next section, the droplet vaporization characteristics will be presented.

3.1 Droplet Vaporization Characteristics

Fig. 3 displays the characteristics of the single droplet vaporization and combustion for the different conditions considered in the present study, cf. Table 2. The temporal evolution of the normalized droplet surface and the mass vaporization rate during the droplet lifetime at different ambient temperature values are shown in Fig. 3a. Fig. 3b displays both the center and the surface temperatures T_{cen} and T_s, respectively. The time t is shown in terms of time divided by the square of the initial droplet diameter, t/d_0^2, to better visualize the results for different initial droplet sizes.

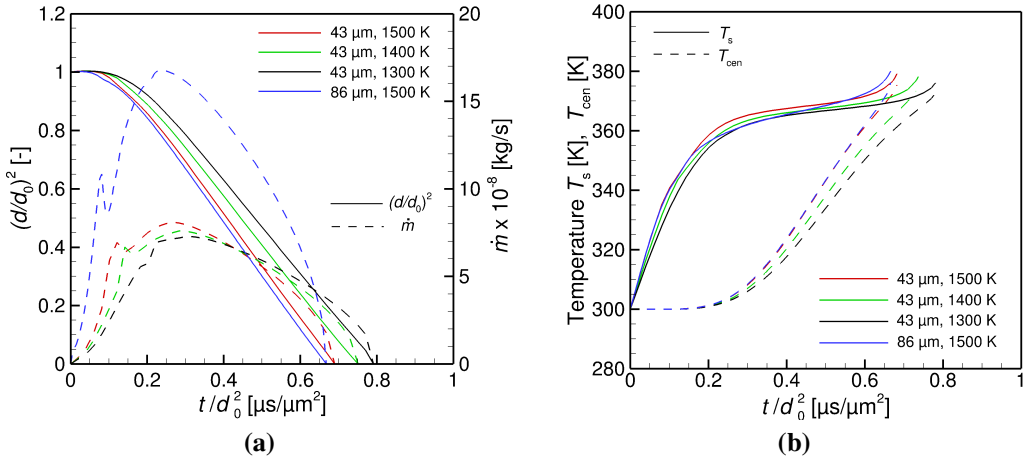

Figure 3: (**a**) Normalized droplet surface, $(d/d_0)^2$ and mass vaporization rate, $\dot{m}$ with time t/d_0^2. (**b**) Droplet surface temperature T_s and center temperature T_{cen} with time t/d_0^2.

The droplet is subjected to hot ambient air, and initially, droplet heating occurs, which results in droplet expansion-this reflects the variable physical properties of the liquid used in the present model. Droplet expansion occurs faster for the highest ambient air temperature and persists over a shorter time compared

to the lower ambient air temperatures, see Fig. 3a. The period of major droplet vaporization constitutes the longest period during the droplet lifetime. As expected, the droplet lifetime increases with a reduction of the initial ambient gas temperature and with an increase in the initial droplet diameter.

The present result of $\tau_d/d_0^2 = 0.69$ μs/μm^2 or $\tau_d = 5.10$ ms (case A) for the droplet lifetime at an ambient temperature of 1500 K and an initial droplet radius of 43 μm may be compared to the numerical result of Kunstmann et al. [4], who also followed the experimental conditions of Li et al. [2], however, they used a constant ambient temperature and did not resolve the gas phase. Their result is approximately 1.2 μs/μm^2 for the ambient oxygen, whereas the experiment gives a value of about 0.54 μs/μm^2; however, in the experiment, spark ignition was used rather than autoignition, so that the experimental value lies below the present computations, which concern autoignition. Moreover, droplet combustion in oxygen is considerably faster than in air, so that the present droplet lifetime lies well in the range of what can be expected considering the different conditions.

Chen et al. [16] suggested the use of a revised d^2 law with an exponent n, d^n law. The initial heating period with droplet expansion, if variable transport properties of the liquid are considered, however, can never be captured by such a simplified law, but may be beneficial for the overall process. In the present study, the strong influence of the Stefan flow and the variable transport properties in the liquid phase, which allow for the prediction of droplet expansion during initial droplet heating, are responsible for the deviation of the results from the d^2 law or any d^n law, as will be further elaborated below.

The profiles of the mass vaporization rate $\dot{m}$ are also shown in Fig. 3a. During droplet heating, the profiles of $\dot{m}$ increase, and they peak at the time when droplet heating is completed. The negative slope in the profile of the mass vaporization rate shows the dominant period of droplet vaporization, where the variable physical properties are reflected in the deviation of a constant slope, which would present the d^2-law. Towards the end of the droplet lifetime, there is an abrupt vaporization which is typical for this process [11]. Roughly between 0.07 and 0.2 μs/μm^2, all profiles of the mass evaporation rate show a non-monotonic behavior which is due to the interaction of the droplet vaporization with the gas phase, which will be addressed in Section 3.3 below.

The profiles of droplet surface temperature, T_s and the temperature at the droplet center, T_{cen} with time are displayed in Fig. 3b. They reflect the characteristics that are expected when the finite thermal conductivity inside the droplet is considered. The boiling temperature of the p-xylene is 420 K, and the figure reveals that the wet-bulb temperature depends on the conditions under consideration. It increases with higher ambient gas temperature and for larger droplet sizes.

The gas-phase characteristics will be studied next.

3.2 Gas-Phase Characteristics

The gas-phase characteristics of the droplet heating and vaporization is displayed exemplarily for the situation of $T_\infty = 1500$ K, and $r_{s,0} = 43$ μm (case A in Table 2). Figs. 4 through 8 show the radial profiles of the major chemical species mass fractions Y_i, where p-xylene is in the vapor phase, and of gas temperature T. Note that $r/r_s = 1$ denotes the position of the droplet surface. In these figures, the left ordinate plotted in black labels shows the mass fraction of p-xylene and O_2, the profiles of which are also in black color, whereas the mass fractions of CO, CO_2, and H_2O are shown on the first ordinate on the right-hand side in blue.

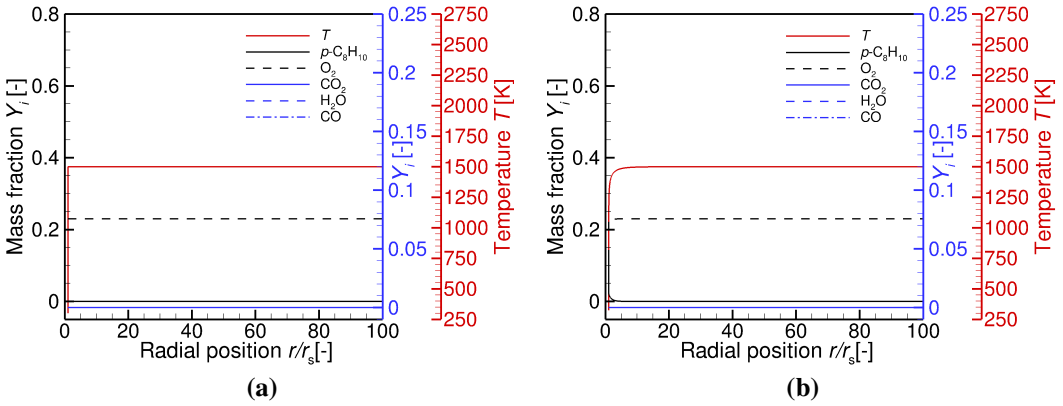

Figure 4: Spatial variation of species mass fractions Y_i and T at (**a**) t/d_0^2 = 0.0 μs/μm^2 and (**b**) t/d_0^2 = 0.05 μs/μm^2.

Fig. 4a displays the initial conditions at t = 0 μs and Fig. 4b at 0.05 μs/μm^2 which is within the droplet heating zone, cf. Fig. 3. At 0.10 μs/μm^2, see Fig. 5a, the peak gas temperature starts rising to a value of 1758 K at r/r_s = 1.85. At this time, an inflection point appears in the temperature profile, and thus, this can be considered as the start of ignition. Note that the ignition time includes the droplet heating and is different from the ignition delay time used in chemical kinetics. The premixed mixture of p-xylene vapor and the O_2 results in chemically controlled reactions at this stage. The species H_2O, CO, and CO_2 start to build up in the chemical reaction zone at ignition.

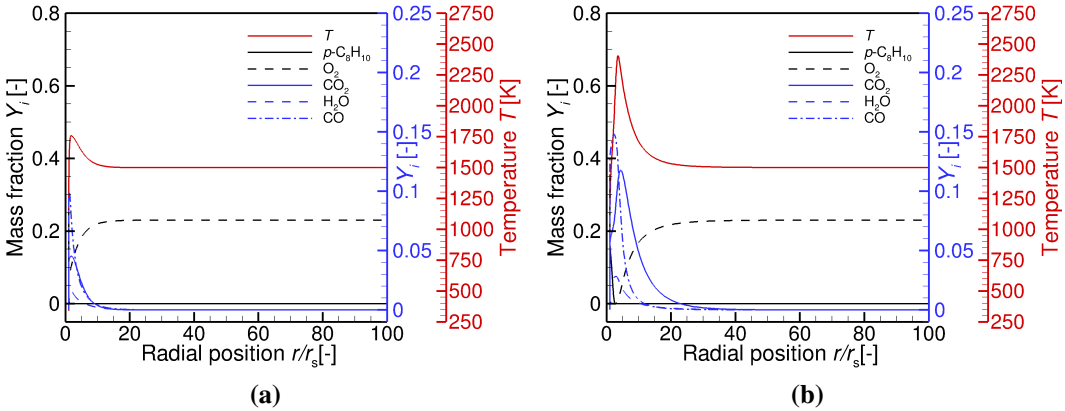

Figure 5: Spatial variation of species mass fractions Y_i and T at (**a**) τ_{ig}/d_0^2 = 0.1 μs/μm^2 and (**b**) t/d_0^2 = 0.15 μs/μm^2.

At 0.15 μs/μm^2, see Fig. 5b, the location of the peak temperature has moved away from the droplet surface to about r/r_s = 3.57 and reaches 2406 K. The species mass fractions of the reaction products increase, where is dominating.

At 0.2 μs/μm^2, see Fig. 6a, the peak temperature rises to 2609 K and its location has moved to about r/r_s = 6.27. A transition from the chemically controlled combustion to diffusion-controlled combustion occurs. As the gas temperature increases, CO_2 is formed and dominates in the high-temperature region where the forward step of the chemical reaction CO + OH $\rightleftharpoons$ CO_2 + H prevails.

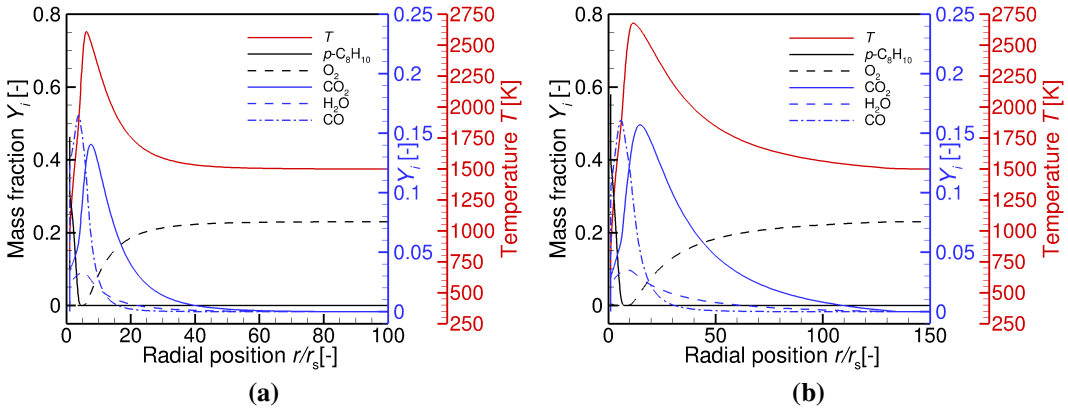

Figure 6: Spatial variation of species mass fractions Y_i and T at (**a**) t/d_0^2 = 0.2 μs/μm^2 and (**b**) t/d_0^2 = 0.5 μs/μm^2.

In Fig. 6b, at 0.50 μs/μm^2, quasi-steady combustion prevails with a rise in peak temperature to 2678 K and a relocation of the flame to r/r_s = 11.58. At 0.69 μs/μm^2, i.e., at the end of the droplet lifetime, see Fig. 7a, the peak temperature drops to 2625 K. This drop in the peak gas temperature is associated with a reduced fuel mass evaporation rate, cf. Fig. 3a, towards the end of droplet lifetime. At this time, the droplet burnout regime is initiated since the flame is no longer fed with fuel vapor. This phase in single droplet combustion has not yet been studied in the literature. The location of the peak temperature has now moved to r/r_s = 23. Fig. 7b shows the species and gas temperature profiles at times after the droplet has completely evaporated, but the chemical reactions still proceed, which is the droplet burnout region. At 0.85 μs/μm^2, the peak temperatures drops to 2003 K. A continuous reduction in the species mass fractions of CO and CO_2 is also observed at these time instants where the burnout occurs.

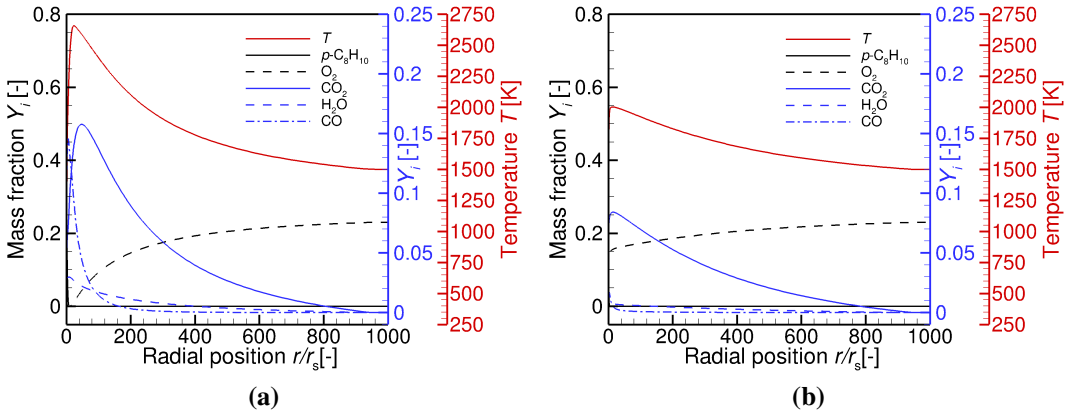

Figure 7: Spatial variation of species mass fractions Y_i and T at (**a**) τ_d/d_0^2 = 0.69 μs/μm^2 and (**b**) t/d_0^2 = 0.85 μs/μm^2.

The droplet combustion simulations are continued after the droplet lifetime until the complete breakdown of the chemical reactions. Fig. 8 displays the radial variation of species mass fractions and gas temperature at time instants after the droplet lifetime. At 1.0 μs/μm^2, see Fig. 8a, the peak temperatures drops to 1691 K and the location of the peak temperature has moved to r/r_s = 9. Further, at 1.5 μs/μm^2, the peak temperature reaches the ambient conditions with complete breakdown of the chemical reactions, terminating the process.

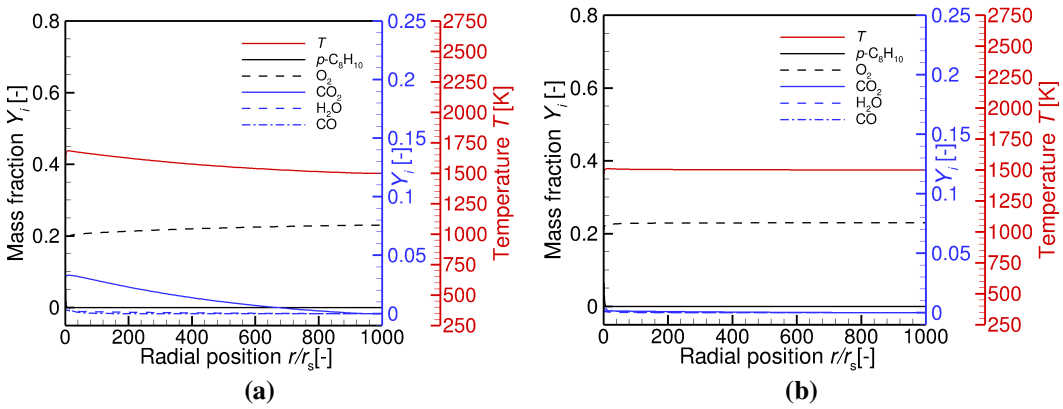

Figure 8: Spatial variation of species mass fractions Y_i and T at (**a**) t/d_0^2 = 1.0 μs/μm^2 and (**b**) t/d_0^2 = 1.5 μs/μm^2.

Fig. 9 shows an overview of the entire process. Fig. 9a displays the temperatures inside the droplet at $r/r_s \leq 1$ (shown in the inset) and the gas temperature in the ambience of the droplet at $r/r_s > 1$. During the droplet heating and before ignition at about 0.05 μs/μm^2, near the droplet surface, the gas temperature decreases from its initial value of 1500 K, and at the ignition instant at 0.10 μs/μm^2, it increases to 1758 K. Thereafter, at 0.15 μs/μm^2 the flame temperature reaches 2406 K and raises to its peak flame temperature of 2678 K at 0.50 μs/μm^2. This is accompanied by an increase in droplet surface temperature and vaporization rate, cf. Fig. 3. At 0.20 μs/μm^2, a transition to the diffusion-controlled combustion occurs, followed by a quasi-steady combustion state. The transition from chemically-controlled to diffusion-controlled combustion occurs when there is a considerable increase in Stefan velocity, (see discussion in Section 3.3), which marks the initiation of remarkable diffusion, which is associated with the local minimum in the profile of the Stefan velocity after autoignition has occurred. At 0.69 μs/μm^2, with reduced mass vaporization rate, see Fig. 3a, a drop in the flame temperature occurs. From 1 μs/μm^2, which corresponds to the post-droplet burnout regime, the chemical reactions slow down, and the ambient temperature approaches the initial gas temperature of 1500 K.

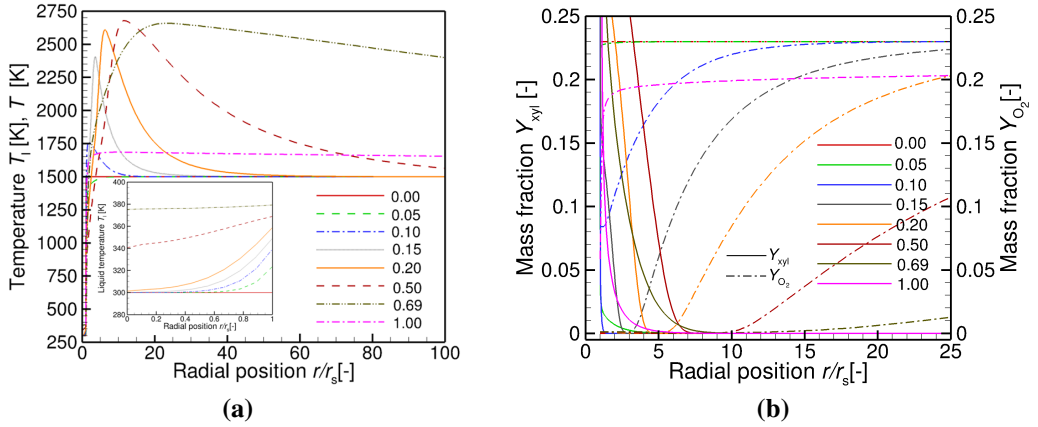

Figure 9: Spatial variation of (**a**) liquid and gas temperatures and (**b**) mass fraction of fuel vapor and of at different times t/d_0^2 in μs/μm^2.

In Fig. 9b, the radial variations of the fuel vapor mass fractions, Y_{xyl} and of Y_{O_2} are shown. The mass fraction of fuel vapor at the droplet surface ranges from 0.6 and is clipped at 0.25 for a better resolution of the

small mass fractions. During droplet heating and initial vaporization, the vapor fraction of *p*-xylene increases drastically near the droplet and distributes from the droplet surface into the ambient due to diffusion effects and the Stefan flow. At the ignition time of 0.10 μs/μm^2, the fuel vapor and O_2 are consumed and reduced in this region. At t/d_0^2 = 0.50 μs/μm^2, the region in the reaction zone where both fuel vapor and O_2 coexist is wider, and the maximum flame temperature prevails as seen in Fig. 9a.

Fig. 10 displays a summary of the four cases studied in the present paper, see Table 2. Fig. 10a gives the peak gas temperature T_{max} plotted against time t/d_0^2 for all conditions under consideration. For all cases, ignition occurs after the initial heating and vaporization of the droplet. A transition from chemically controlled combustion to diffusion-controlled combustion occurs, resulting in quasi-steady combustion. The predictions of the flame temperature are in line with the predictions of *n*-heptane droplet combustion for different droplet diameters and ambient temperature values [27]. Also, the larger initial droplet size and higher ambient temperature result in the highest flame temperature among the different cases considered. Towards the end of droplet lifetime, a reduction in the flame temperature occurs, which is more pronounced in the smaller droplet due to the lower amount of fuel vapor from the smaller droplet. After complete evaporation of the droplet, the peak temperature drops for all the cases, gradually leading to the complete breakdown of the chemical reactions.

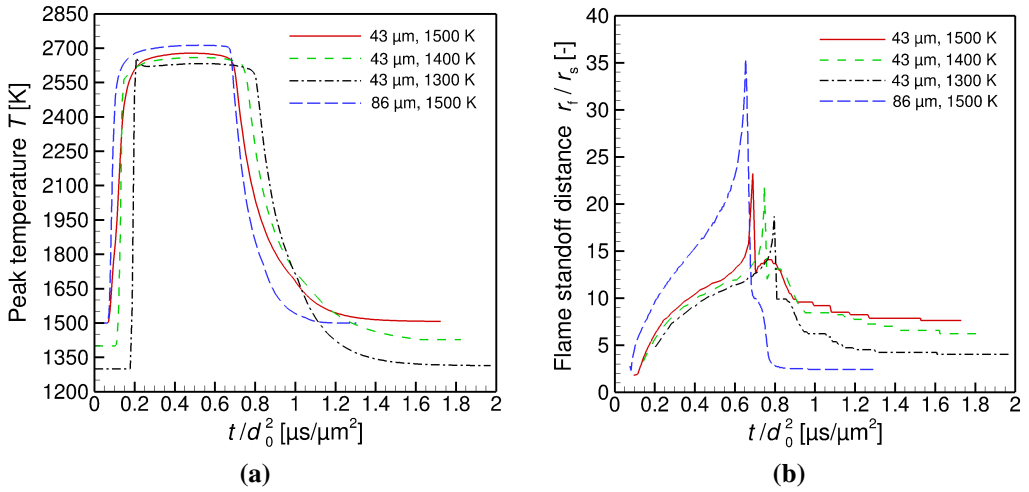

Figure 10: (**a**) Peak gas temperature T_{max} and (**b**) flame standoff distance r_f/r_s with time t/d_0^2.

The profiles of the gas temperatures reflect the characteristics of the time scales provided in Table 2. The strong increase in gas temperature marks the ignition time τ_{ig}. The lowest ambient gas temperature shows a strong delay in ignition time, which results in a local maximum of the flame temperature at ignition. The quasi-steady vaporization period is characterized by an almost constant flame temperature before it dramatically decreases due to a lack of fuel vapor that results from the end of the droplet vaporization marked by the droplet lifetime τ_d. The values τ_d/d_0^2 in Table 2 confirm that the initial droplet size has a significant influence on the droplet lifetime, in contrast to the ambient gas temperature. The total process time τ_t is considerably longer for lower ambient temperatures and larger droplets. However, τ_t/d_0^2 is shortest for the largest initial droplet, which is associated with the shortest values of τ_{ig}/d_0^2, τ_d/d_0^2, and τ_t/d_0^2. The droplet surface temperature for the largest droplet increases fastest, see Fig. 3, causing a short ignition time which is associated with a fast rise in gas temperature seen in Fig. 10a.

This also affects the flame standoff distance, which is taken as the position of the maximum flame temperature r_f normalized by the instantaneous droplet radius r_s, see Fig. 10b. Ignition occurs near the

droplet surface at $r/r_s = 1$. The flame standoff distance of p-xylene droplet increases throughout the droplet lifetime, which is also reported for n-heptane droplets [27]. At later times beyond the droplet lifetime, the flame moves closer to the droplet surface due to a shortage of fuel vapor, resulting in a decrease in peak temperature, see Fig. 10a. The flame standoff distance is largest for the biggest droplet and reduces with ambient gas temperature.

3.3 Interaction of Vaporization and Ignition

The non-monotonic behavior of the mass evaporation rate shown in Fig. 3a is addressed in this section. For this purpose, the vaporization rate constant $K = -\frac{dd_s^2}{dt} = -8r_s\frac{dr_s}{dt}$ with time t/d_0^2, where $d_s = 2r_s$ is the instantaneous droplet diameter, is shown in Fig. 11a. For all cases, K initially decreases slightly due to droplet expansion. Most often, this phase is not shown in literature [28] since droplet expansion is only visible when variable liquid properties are used in simulations. After droplet expansion, see Fig. 3a, the vaporization rate constant increases during droplet heating, reaching a maximum where a quasi-steady phase is seen during which the vaporization rate constant attains a plateau-like behavior. At the end of the droplet lifetime, the vaporization rate constant abruptly decreases to zero. A small oscillatory change in K occurs after the ignition and is most significant for the larger droplet diameter. The strong variation of the vaporization rate constant K confirms that a constant value as used in approximations with the d^2 law is not appropriate, particularly during droplet expansion and heating.

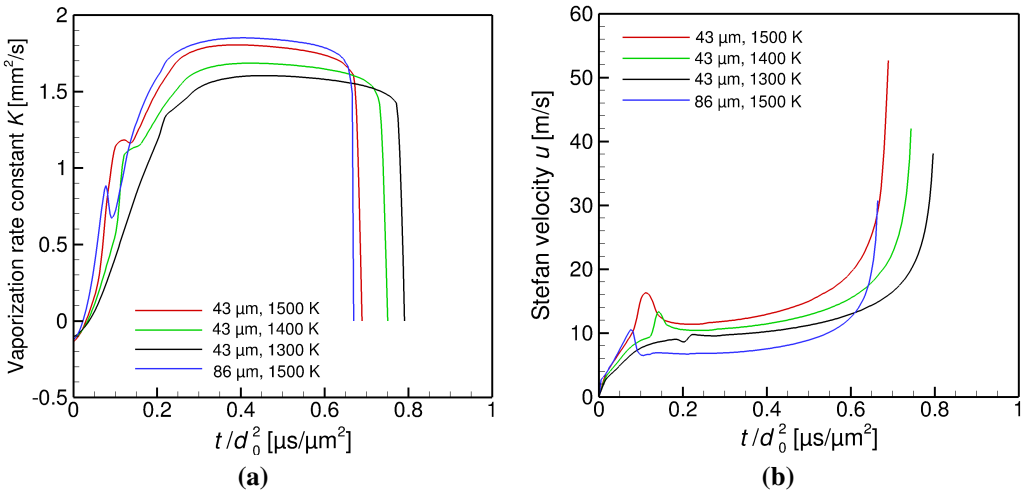

Figure 11: (**a**) Vaporization rate constant K and (**b**) Stefan velocity u with time t/d_0^2.

Fig. 11b shows the temporal variation of Stefan velocity for the cases under consideration. An initial rise in the Stefan velocity is followed by an almost constant period during quasi-steady droplet vaporization, and towards the end of droplet lifetime, a sudden rise occurs. As expected, the Stefan velocity is lower for larger droplet sizes and increases with higher ambient gas temperature.

The experimental work by Chauveau et al. [29] on n-decane droplet vaporization in a hot atmospheric environment also predicts non-monotonicity in the mass vaporization rate $\dot{m}$ for the larger droplet size, and they attributed this to the lower Stefan flow velocity that causes vapor accumulation and thus reduces the mass evaporation rate. Awasthi et al. [28] performed numerical simulations for the auto-ignition of methanol droplet combustion, and they predicted a significant variation of vaporization rate constant K during the droplet lifetime. An oscillatory change in K is observed after the droplet ignition, and they attributed it to the

changes in the surface composition arising from internal circulation of the droplet. Fang et al. [30] carried out experimental and theoretical studies to demonstrate the deviation of d^2 law during droplet combustion for various liquid hydrocarbon fuels under the influence of gravity. They attributed their deviation to the coupled effects of momentum, heat, and mass transfer that result in the non-quadratic shrinkage law. Chen et al. [16] reported the deviation of the d^2 law in their droplet combustion studies under gravity conditions, and the deviation of their results was argued to result from the simultaneous momentum, heat, and mass transfer from the buoyant convection set up by the flame around the droplet. In the present study, the rapid droplet vaporization in hot air conditions is associated with a significant Stefan flow velocity, which influences the vaporization rate constant. Moreover, it will be shown below that the chemical reactions also contribute to a deviation of the vaporization rate constant from the d^2 law.

All droplet characteristics, including the Stefan velocity, the vaporization rate constant, and the mass vaporization rate, show a non-monotonic, somewhat oscillatory behavior around the time when ignition occurs. To analyze the effect of chemical kinetics on these profiles, the p-xylene consumption rate of the chemical reactions $\dot{\omega}_{C_8H_{10}}$ and heat release rate $\dot{Q} = -\sum_{k=1}^{N} M_k \dot{\omega}_k h_k$ during ignition are discussed further for case D, cf. Table 2, where this effect is most significant.

The chemical reactions for the consumption of p-xylene are:

$$C_8H_{10} + O \rightarrow 0.5C_2H_4 + C_7H_7 + OH \quad \text{(R1)}$$

$$C_8H_{10} + OH \rightarrow 0.5C_2H_4 + C_7H_7 + H_2O \quad \text{(R2)}$$

$$C_8H_{10} + H \rightarrow 0.5C_2H_4 + C_7H_7 + H_2 \quad \text{(R3)}$$

$$C_8H_{10} + O_2 \rightarrow 0.5C_2H_4 + C_7H_7 + HO_2 \quad \text{(R4)}$$

$$C_8H_{10} + M \rightleftharpoons CH_3 + C_2H_4 + M \quad \text{(R5)}$$

From these reactions, (R1), (R2), and (R3) in which the fuel reacts with the radicals O, OH, and H are most significant and are plotted against radial position at six different times, see Fig. 12. (R3) with its lowest impact increases during the first time steps, whereas (R1) and (R2) show an initial increase and decrease thereafter. The reaction of the fuel vapor with OH is most important, followed by that with the O-radical. At later times, the reaction with H becomes more important.

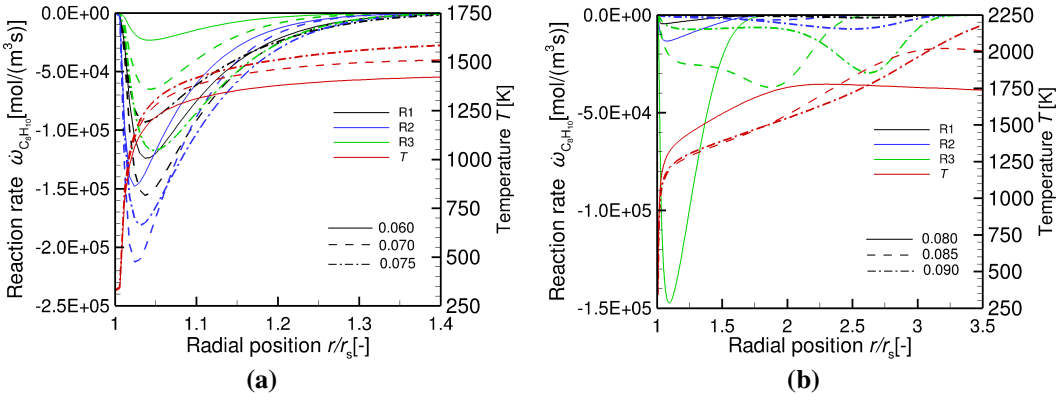

Figure 12: Spatial variation of the chemical reaction rate of p-xylene $\dot{w}_{C_8H_{10}}$ (**a**) during ignition and (**b**) after ignition for case D in Table 2 at different times t/d_0^2 in μs/μm^2.

At 0.06 μs/μm^2, i.e., prior to the droplet ignition, Fig. 12a shows that the chemical kinetics control the process. At this time, the chemical reactions occur near the droplet surface. Further, at time 0.085 μs/μm^2

and beyond, see Figs. 12b and 13a, the chemical reaction zone moves away from the droplet surface and a transition to diffusion-controlled combustion occurs with a sharp rise in the gas phase temperature. This transition behavior can influence the droplet vaporization at these times and the oscillatory change in the profiles of K, $\dot{m}$, and the Stefan velocity u occurs, see Figs. 3a and 11a,b.

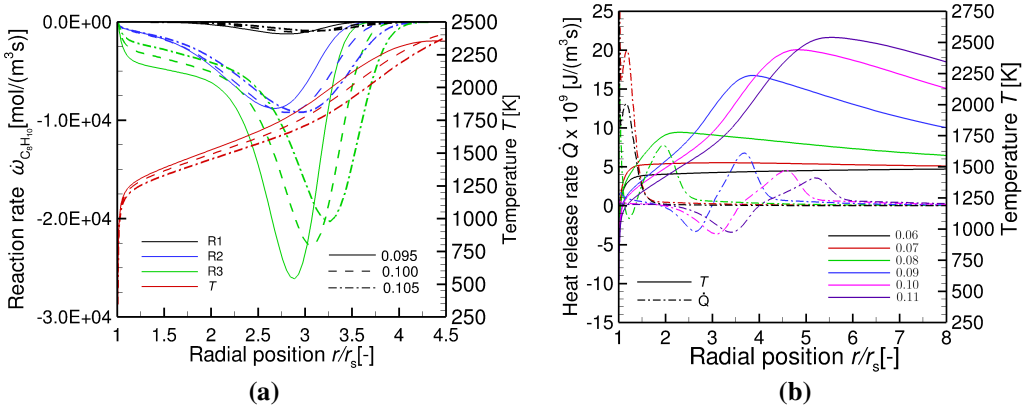

Figure 13: Spatial variation of (**a**) chemical reaction rate of p-xylene $\dot{w}_{C_8H_{10}}$ after ignition and (**b**) heat release rate $\dot{Q}$ for case D in Table 2 at different times t/d_0^2 in μs/μm^2.

Fig. 13b displays the profile of the heat release rate $\dot{Q}$ at different times for case D in Table 2. At 0.06 μs/μm^2, i.e., prior to ignition, a significant positive $\dot{Q}$ value exists near the droplet surface. Further, at the ignition time of 0.07 μs/μm^2, a sharp rise in the heat release rate occurs, indicating an intense chemical activity with energy-releasing reactions near the droplet surface. After ignition, a drop in $\dot{Q}$ within the positive region and at certain radial locations, the $\dot{Q}$ takes negative values. The negative values of $\dot{Q}$ are associated with the energy-absorbing chemical reactions after ignition.

Thus, the initial chemical reactions consuming the p-xylene vapor have a pronounced impact on the droplet vaporization characteristics, leading to some oscillation in the profiles of the mass vaporization rate, the Stefan velocity, and the vaporization constant. In reverse, the vaporization of the droplet enables the ignition through the formation of fuel vapor, which feeds the flame. After the completion of droplet vaporization, the combustion is sustained, retards, and eventually breaks down due to a lack of fuel vapor.

The present numerical simulations of pure p-xylene droplet auto-ignition and combustion with detailed chemical kinetics are novel. The model predictions include the temporal variation of the Stefan velocity during the droplet lifetime. Moreover, a new analysis of the interaction between the droplet ignition and vaporization, the temporal variation of the peak temperature, and flame standoff ratio is presented all the way until the chemical reactions break down completely due to a lack of combustible fuel vapor.

The one-dimensional model assumed in the present study has some limitations in neglecting the effects of possible asymmetric droplet behavior, which may occur under gravity or buoyancy. The detailed chemical reaction scheme does not include soot formation even though its precursors are included. Also, the assumption of a lack of radiation may lead to too high flame temperature for the larger droplet sizes. These differences may affect the standoff distance of the flame as well.

The present study builds the ground for further simulations considering the detailed chemistry in the droplet heating, vaporization, and combustion of p-xylene in air, which will be used in future studies of soot formation and nanoparticle formation in the bi-component flame spray pyrolysis of the precursor solution of TTIP/p-xylene.

4 Conclusions

A detailed one-dimensional model for the simulation of the heating, vaporization, autoignition, and combustion of single spherically-symmetric *p*-xylene droplets in air was developed. The model accounts for single droplet heating and vaporization, and the variable liquid properties allow for the prediction of droplet expansion during the heating. A detailed chemical reaction scheme with some complex reactions was incorporated into the model, where 25 chemical species and 93 chemical reactions are used.

A parameter study was performed with ambient air temperatures of 1500, 1400, and 1300 K for droplets with an initial radius of 43 μm. Additionally, at 1500 K, the initial droplet radius was doubled. These conditions followed the experimental investigation in the literature, but the results cannot be compared to their work because spark ignition was used in the experiment, and the ambience was pure oxygen. However, reasonable qualitative agreement was found with their results.

The simulations were conducted throughout the entire process–from initial droplet heating and vaporization, autoignition in the gas phase, quasi-steady combustion, including the burnout following the droplet lifetime, until all the chemical reactions break down. The latter process has not yet been studied in literature and is a novel contribution of the present work. Concerning the liquid phase characteristics, the simulations show commonly observed droplet expansion during initial heating, which reflects the temperature-dependent liquid phase properties. Moreover, the dependence of the wet-bulb temperature on the above conditions is confirmed.

It was shown that the autoignition in the gas phase has a pronounced effect on the vaporization characteristics of the droplets. A non-monotonicity in the temporal evolution of the Stefan velocity, the mass vaporization rate, and the vaporization rate constant during autoignition is indicative of the interaction of ignition and vaporization. Previous numerical studies on the autoignition of methanol droplets reported a non-monotonic behavior in the vaporization rate constant after the ignition instant, and they attributed this to the internal circulation of the droplet, which is absent in the present study. Experimental investigations on *n*-decane droplet vaporization also observed fluctuations in the vaporization rate constant following the droplet ignition, which was attributed to the reduced evaporation velocity. From the temporal evolution of the Stefan velocity, the vaporization rate constant, the flame temperature, and flame standoff distance, the deviation from simple models such as the d^2 law is obvious for *p*-xylene droplet evaporation and combustion in the present study. This is in agreement with other studies, which also reported the defying d^2 law.

The use of the present detailed chemical reaction mechanism allows for the prediction of intermediates and particularly of soot precursors, even though the soot formation itself is not addressed. An experimental study reported the sooting tendency of *p*-xylene, and future simulations may extend the present study to account for the soot formation.

In the present work, the assumption of spherical symmetric droplets in the one-dimensional model restricts the model to microgravity conditions in the absence of natural and forced convection. Since thermal radiation effects are not considered, the predicted gas temperature might be somewhat too high for the large droplet.

An extension of the present work to the bi-component precursor solution droplets of TTIP and *p*-xylene with detailed chemistry and with possible consideration of puffing and micro-explosions will enable the investigation of TiO_2 nanoparticle formation in the gas phase.

Acknowledgement: The authors thank Dr. Monika Nanjaiah and Prof. Irenaeus Wlokas from the University of Duisburg–Essen, Germany, for providing the chemical reaction mechanism for *p*-xylene in air.

Funding Statement: Financial support of the German Research Foundation (DFG) through SPP 1980, grant GU 255/13-2 is gratefully acknowledged.

Author Contributions: The authors confirm contribution to the paper as follows: Conceptualization, Sachin Tom and Eva Gutheil; methodology, Sachin Tom and Eva Gutheil; formal analysis, Sachin Tom; resources, Eva Gutheil; writing—original draft preparation, Sachin Tom and Eva Gutheil; writing—review and editing, Sachin Tom and Eva Gutheil; visualization, Sachin Tom; supervision, Eva Gutheil; project administration, Eva Gutheil; funding acquisition, Eva Gutheil. All authors reviewed and approved the final version of the manuscript.

Availability of Data and Materials: The data are available on request.

Ethics Approval: Not applicable.

Conflicts of Interest: The authors declare no conflicts of interest.

References

1. Dimitriou C, Psathas P, Solakidou M, Deligiannakis Y. Advanced flame spray pyrolysis (FSP) technologies for engineering multifunctional nanostructures and nanodevices. Nanomaterials. 2023;13(23):3006. doi:10.3390/nano13233006.
2. Li H, Rosebrock CD, Riefler N, Wriedt T, Mädler L. Experimental investigation on microexplosion of single isolated burning droplets containing titanium (IV) isopropoxide for nanoparticle production. Proc Combust Instit. 2017;36(1):1011–8. doi:10.1016/j.proci.2016.09.017.
3. Narasu P, Gutheil E. A new model for puffing and micro-explosion of single titanium(IV) isopropoxide/p-xylene precursor solution droplets. Int J Heat Mass Transf. 2023;202(11):123647. doi:10.1016/j.ijheatmasstransfer.2022.123647.
4. Kunstmann B, Wlokas I, Kohns M, Hasse H. Simulation study of superheating in evaporating droplets of (TTIP+*p*-xylene) in spray flame synthesis. Appl Energy Combust Sci. 2023;15(8):100156. doi:10.1016/j.jaecs.2023.100156.
5. Spalding DB. The combustion of liquid fuels. In: Fourth Symposium (International) on Combustion. Baltimore: Williams and Wilkins; 1953. p. 847–64. doi:10.1016/S0082-0784(53)80110-4.
6. Sirignano WA. Fluid dynamics and transport of droplets and sprays. Cambridge, UK: Cambridge University Press; 2010.
7. Law CK. Recent advances in droplet vaporization and combustion. Progress Energy Combust Sci. 1982;8(3):171–201. doi:10.1016/0360-1285(82)90011-9.
8. Dietrich DL, Struk PM, Ikegami M, Xu G. Single droplet combustion of decane in microgravity: experiments and numerical modelling. Combust Theory Model. 2005;9(4):569–85. doi:10.1080/13647830500256039.
9. Marchese AJ, Dryer FL, Nayagam V. Numerical modeling of isolated *n*-alkane droplet flames: initial comparisons with ground and space-based microgravity experiments. Combust Flame. 1999;116(3):432–59. doi:10.1016/S0010-2180(98)00109-6.
10. Cho SY, Yetter RA, Dryer FL. A computer model for one-dimensional mass and energy transport in and around chemically reacting particles, including complex gas-phase chemistry, multicomponent molecular diffusion, surface evaporation, and heterogeneous reaction. J Comput Phys. 1992;102(1):160–79. doi:10.1016/S0021-9991(05)80013-0.
11. Marchese AJ, Dryer FL. The effect of liquid mass transport on the combustion and extinction of bicomponent droplets of methanol and water. Combust Flame. 1996;105(1):104–22. doi:10.1016/0010-2180(95)00179-4.
12. Cuoci A, Mehl M, Buzzi-Ferraris G, Faravelli T, Manca D, Ranzi E. Autoignition and burning rates of fuel droplets under microgravity. Combust Flame. 2005;143(3):211–26. doi:10.1016/j.combustflame.2005.06.003.
13. Cuoci A, Cipriano E, Saufi AE, Frassoldati A. A numerical framework for modeling evaporation and combustion of isolated, spherically-symmetric, multi-component fuel droplets. J Comput Sci. 2024;83(8):102453. doi:10.1016/j.jocs.2024.102453.

14. Giusti A, Sidey JAM, Borghesi G, Mastorakos E. Simulations of droplet combustion under gas turbine conditions. Combust Flame. 2017;184(4):101–16. doi:10.1016/j.combustflame.2017.01.026.
15. Zhang W, Zhou H, Liu YC. Autoignition regime boundaries for *n*-heptane droplets under microgravity. Microgravity Sci Technol. 2022;34(4):57. doi:10.1007/s12217-022-09965-0.
16. Chen YA, Chiang CH, Yang CY, Yang SY, Wei HH. Defying the d^2-law in fuel droplet combustion under gravity. Phys Fluids. 2024;36(9):097171. doi:10.1063/5.0225223.
17. Ren Y, Cai J, Pitsch H. Theoretical single-droplet model for particle formation in flame spray pyrolysis. Energy Fuels. 2021;35(2):1750–9. doi:10.1021/acs.energyfuels.0c03669.
18. Rosebrock CD, Riefler N, Wriedt T, Mädler L, Tse SD. Disruptive burning of precursor/solvent droplets in flame-spray synthesis of nanoparticles. AIChE J. 2013;59(12):4553–66. doi:10.1002/aic.14234.
19. Shang W, Cao J, Yang S, He Z. In-flame soot quantification of *n*-hexadecane droplets using diffused back-illumination extinction imaging. Case Stud Therm Eng. 2022;30:101699. doi:10.1016/j.csite.2021.101699.
20. Nanjaiah M, Roderigo K, Janbazi H, Peukert S, Eigemann J, Kempf A, et al. Compact, global-skeletal reaction mechanisms for combustion of *o*-xylene/air and 1-butanol/air. Energy Fuels. 2023;37(23):19188–95. doi:10.1021/acs.energyfuels.3c02995.
21. Ranzi E, Frassoldati A, Grana R, Cuoci A, Faravelli T, Kelley AP, et al. Hierarchical and comparative kinetic modeling of laminar flame speeds of hydrocarbon and oxygenated fuels. Progress Energy Combust Sci. 2012;38(4):468–501. doi:10.1016/j.pecs.2012.03.004.
22. Narasu P, Nanjaiah M, Wlokas I, Gutheil E. Numerical simulation and parameterization of the heating and evaporation of a titanium (IV) isopropoxide/*p*-xylene precursor/solvent droplet in hot convective air. Int J Multiphase Flow. 2022;150(9):104006. doi:10.1016/j.ijmultiphaseflow.2022.104006.
23. Ying Z, Gutheil E. Numerical simulation of TTIP*p*-xylene precursor solution spray flames in the counterflow configuration. Appl Energy Combust Sci. 2023;15(6):100161. doi:10.1016/j.jaecs.2023.100161.
24. Keller A, Wlokas I, Kohns M, Hasse H. Thermophysical properties of mixtures of titanium (IV) isopropoxide and *p*-xylene. J Chem Eng Data. 2020;65(2):869–76. doi:10.1021/acs.jced.9b01059.
25. Rao PM, Raghavan V, Velusamy K, Sundararajan T, Shet USP. Modeling of quasi-steady sodium droplet combustion in convective environment. Int J Heat Mass Transf. 2012;55(4):734–43. doi:10.1016/j.ijheatmasstransfer.2011.10.036.
26. Aouina Y, Maas U, Gutheil E, Riedel U, Warnatz J. Mathematical modeling of droplet heating, vaporization, and ignition including detailed chemistry. Combust Sci Technol. 2001;173(1):1–23. doi:10.1080/00102200108935842.
27. Awasthi I, Pope DN, Gogos G. Effects of the ambient temperature and initial diameter in droplet combustion. Combust Flame. 2014;161(7):1883–99. doi:10.1016/j.combustflame.2014.01.001.
28. Awasthi I, Gogos G, Sundararajan T. Effects of size on combustion of isolated methanol droplets. Combust Flame. 2013;160(9):1789–802. doi:10.1016/j.combustflame.2013.03.023.
29. Chauveau C, Birouk M, Gökalp I. An analysis of the d^2-law departure during droplet evaporation in microgravity. Int J Multiphase Flow. 2011;37(3):252–9. doi:10.1016/j.ijmultiphaseflow.2010.10.009.
30. Fang CA, Yang CY, Yang SY, Wei HH. Revisiting droplet combustion: a nearly universal shrinkage kinetic law driven by flame-induced buoyant convection. J Fluid Mech. 2025;1025:A15. doi:10.1017/jfm.2025.10880.